

**Babes-Bolyai University**  
**Faculty of Physics**

Doctoral Thesis Summary

**Designing new chitosan-coated plasmonic  
nanoparticles for biomolecular sensing and  
antibacterial activity**

by

**Monica Potara**

**Scientific Advisor**  
**Prof. Dr. Simion Astilean**

CLUJ-NAPOCA  
2012

## **Introduction**

### **Chapter 1: Literature Review**

1.1. Noble-metal nanoparticles and their properties .....	3 -
1.1.1. Surface plasmon absorption and scattering of noble-metal nanoparticles.....	3 -
1.2. Biomedical applications of noble-metal nanoparticles .....	3 -
1.2.1. Biosensing based on colloidal aggregation.....	3 -
1.2.2. Biosensing based on LSPR shift .....	3 -
1.2.3. Biosensing based on surface-enhanced Raman scattering .....	4 -
1.2.4. Antibacterial activity of silver nanoparticles .....	4 -
1.3. Chitosan biopolymer: properties and biomedical applications .....	5 -

### **Chapter 2: Gold-Chitosan Nanocomposites: Synthesis and Characterization**

2.1. Gold nanoparticles formation in chitosan solution .....	6 -
2.2. Study of gold nanoparticle formation in chitosan solution at different reaction temperatures .....	7 -
2.3. Study of the stability of as prepared gold-chitosan nanocomposites .....	9 -

### **Chapter 3: Chitosan Mediated Synthesis of Anisotropic Silver Nanoparticles**

3.1. The growth of triangular nanoplates .....	10 -
3.1.1. First step: Preparation of seeds solution .....	10 -
3.1.2. Second step: The growth of triangular silver nanoplates.....	10 -
3.1.3. Morphology analysis by TEM .....	10 -
3.1.4. Surface plasmon resonances of triangular silver nanoplates .....	11 -
3.2. Tuning the size and morphology of silver nanoparticles .....	12 -
3.2.1. The effect of trisodium citrate on the nanoparticle size and morphology .....	12 -
3.2.2. The effect of chitosan concentration on the nanoparticle size and morphology..	14 -
3.3. Stability of as prepared chitosan-silver nanocomposites .....	14 -
3.3.1. FT-IR characterization .....	14 -
3.3.2. Study of the chitosan-silver nanocomposites stability under a wide range of environmental conditions.....	15 -

### **Chapter 4: Chitosan-Coated Anisotropic Silver Nanoparticles as Versatile**

#### **LSPR-SERS Plasmonic Sensors**

4.1. Chitosan-coated anisotropic silver nanoparticles as dual LSPR- SERS plasmonic sensors in solution.....	16 -
4.1.1. LSPR bulk refractive index (RI) sensitivity.....	16 -
4.1.2. LSPR surface sensitivity .....	17 -
4.1.3. SERS sensitivity.....	18 -
4.2. Chitosan-coated anisotropic silver nanoparticles for SERS detection at single molecule level .....	19 -
4.2.1. Morphological and optical characterization of SERS substrates .....	19 -
4.2.2. Ensemble-averaged SERS of adenine.....	21 -
4.2.3. Single-molecule SERS of adenine .....	23 -

### **Chapter 5: Synergistic Antibacterial Activity of Chitosan-Silver Nanocomposites on**

#### ***Staphylococcus aureus***

5.1. MIC and MBC determination .....	25 -
5.2. AFM imaging of the antibacterial effects of silver nanoparticles on <i>S. aureus</i> .....	26 -
5.3. SERS measurements .....	27 -

<b>Conclusions</b> .....	28 -
--------------------------	------

<b>References</b> .....	28 -
-------------------------	------

# Introduction

The major aim of this thesis is to design anisotropic chitosan noble-metal nanocomposites with tunable plasmonic resonances, which can serve as versatile plasmonic biosensors and effective antibacterial agents.

The thesis is structured into six chapters. **Chapter 1** presents a short review of the scientific literature regarding the biomedical applications of noble-metal nanoparticles. A brief discussion on optical properties of metal nanoparticles is introduced. We point out the limitation of spherical particles, and, further introduced the anisotropic nanoparticles.

In **Chapter 2** we present a clean, nontoxic, environmentally friendly synthesis procedure to generate a large variety of gold nanoparticles by using chitosan, a biocompatible, biodegradable, natural polymer, as reducing and stabilizing agent. The formation of gold–chitosan nanocomposites is characterized by UV–vis absorption spectroscopy, transmission electron microscopy (TEM), X-ray diffraction (XRD), Raman and Fourier transform infrared (FT-IR) measurements.

In **Chapter 3** we introduce a new, two-step approach to prepare anisotropic silver nanoparticles enveloped in a shell of chitosan biopolymer. The morphology and optical properties of as prepared bionanocomposites are characterized by UV-VIS-NIR extinction spectroscopy, TEM, XRD, electron diffraction (ED), Raman and FT-IR measurements. By performing a series of well-designed experiments we demonstrate that the plasmonic resonances of as prepared nanoparticles are tunable throughout the visible and near infrared (NIR) region of the spectrum.

**Chapter 4** is divided into two parts. In the first part, taking the advantage of the high stability of chitosan-coated silver nanoparticles in combination with their optical response tunability, we integrate the localized surface plasmon resonance (LSPR) with surface-enhanced Raman scattering (SERS) sensing on plasmonic nanoparticles in solution-phase. In a second part of this chapter, we demonstrate that small ensembles of anisotropic silver nanoparticles trapped within thin films of chitosan enable single-molecule detection by SERS.

In **Chapter 5** we investigate the possible synergistic combination of chitosan and silver nanoparticles with the aim to identify a new, biocompatible material with enhanced antibacterial properties. Comparative studies are performed to test the impact of row nanoparticles, chitosan-silver composites and chitosan biopolymer against two representative methicillin-resistant *Staphylococcus aureus* (*S. aureus*) strains.

In **Chapter 6** of this thesis the conclusions and perspectives of my studies are presented.

**Keywords:** *noble metal nanoparticles, chitosan, localized surface plasmon resonances (LSPR), surface enhanced-Raman spectroscopy (SERS), antibacterial agent.*

# Chapter 1

## Literature Review

### 1.1. Noble-metal nanoparticles and their properties

#### 1.1.1. Surface plasmon absorption and scattering of noble-metal nanoparticles

When the size of a material approaches the nanoscale, its physical and chemical properties change dramatically. The most spectacularly phenomenon that is manifested is the bright color of colloidal nanoparticles, which is the result of electromagnetic interactions between incident light and conduction electrons in metal nanoparticles. Actually the incoming light couples with the oscillation frequency of the conduction electrons in noble metal nanoparticles and a so-called *surface plasmon resonance* (SPR) arises, which is manifested as a strong UV–visible absorption band [1]. In the case of metal nanoparticles these SPR are localized on the nanoparticle’s surface and are called *localized surface plasmon resonances* (LSPR).

### 1.2. Biomedical applications of noble-metal nanoparticles

The exceptional chemical, electronic and plasmonic properties of metallic nanoparticles make them very attractive in a variety of biomedical applications such as: molecular sensing, molecular diagnosis, antibacterial action, drug delivery, cancer therapy etc. [2].

#### 1.2.1. Biosensing based on colloidal aggregation

The high sensitivity of the LSPR location and intensity to small changes in the dielectric medium around the particle is particularly attractive for sensing applications. Depending on the origin of the LSPR changes, one can distinguish two types of sensors: (1) colorimetric (aggregation) sensors, and (2) refractive index (RI) sensors. In the first case, the adsorption of molecules onto the nanoparticles surface induces the aggregation of the particles, a phenomenon accompanied by a drastic color change of colloidal solution. Therefore, the detection can be easily visualized with the naked eye. Colloidal aggregation has been widely used for detection of biologically relevant molecules such as DNA, antibodies, etc. [3].

#### 1.2.2. Biosensing based on LSPR shift

The second class of sensors relates on the LSPR shift, determined by a change of the refractive index around the nanoparticles. In this case the detection can be spectroscopically monitored via the LSPR peak shift. There are two kinds of change in the environment of a nanoparticle that are of interest: (1) a bulk change, when the entire environment of the nanoparticle is

modified, and (2) a local change, when only a molecular layer is adsorbed onto the nanoparticle. The latter definition has particular significance within biosensing, where typically either direct adsorption of molecules onto a nanoparticle or adsorption onto a receptor or host molecule induces the LSPR shift. The first demonstration where refractive index sensors were used for detection of biologically relevant molecules is the biotin-streptavidin model couple [4]. Since then, the sensing strategy based on the LSPR shift has drawn a great deal of attention.

### ***1.2.3. Biosensing based on surface-enhanced Raman scattering***

The ability to identify and provide structural information about molecular species in low concentration renders surface-enhanced Raman spectroscopy (SERS) an excellent tool for ultrasensitive detection, analysis and imaging of biological samples [5]. SERS largely relies on collective oscillations of conduction electrons excited by light on the surface of noble-metal nanoparticles, which significantly enhances the optical near fields. This in turn, enhances the Raman scattering from molecules located in this region [6]. It is generally accepted that enormous Raman signal enhancement arises mainly from the electromagnetic (EM) effect as stated before. Particularly, when an analyte is adsorbed onto so-called *hot-spots*, such as gaps and junctions created between interconnected nanoparticles, its Raman signal can be drastically amplified, resulting in an enhancement factor strong enough to allow single molecule detection. The chemical charge transfer (CT) that occurs between the adsorbed molecule and the metal conduction band is the second main effect, which may also contribute to the overall SERS signal. While the EM effect extends a certain distance beyond the surface, the CT mechanism is operational only if the analyte molecules directly adsorb onto the metal surface.

### ***1.2.4. Antibacterial activity of silver nanoparticles***

Silver nanoparticles exhibit antibacterial activity against Gram-negative and Gram-positive bacteria which was exploited in a number of studies. However, their mechanism of toxicity is still only partially solved. Several studies suggest that silver nanoparticles interact with the cell membrane and some of them also penetrate the bacterial cell wall, thereby causing the death of bacteria [7]. Some hypotheses indicate that the antimicrobial mechanism of silver nanoparticles is mediated by the formation of free radicals which induce damage to the bacterial membrane, resulting in cell death [8]. Another mechanism suggests that the antimicrobial activity of nanoparticles is brought about by the action of the ions released by the nanoparticles [9]. A generally accepted idea is that the antimicrobial activity of silver nanoparticles strongly depends on several parameters such as their size, shape, and stability in the growth medium.

### 1.3. Chitosan biopolymer: properties and biomedical applications

Chitosan is a ( $\beta$ -1, 4)-linked D-glucosamine, N-deacetylated derivative of chitin, the most abundant natural polymer after cellulose, constituting the exoskeleton of arthropods and cell walls of fungi and yeast [10]. Chitosan is obtained by partial deacetylation of chitin (at least 50%), as represented schematically in Figure 1-1. Therefore, chitosan is a natural, biocompatible, biodegradable polymer which displays an excellent film-forming ability, high mechanical strength, and a susceptibility to chemical modifications. Because chitin deacetylation is incomplete, chitosan is a copolymer composed of glucosamine and N-acetylglucosamine (see Figure 1-1).

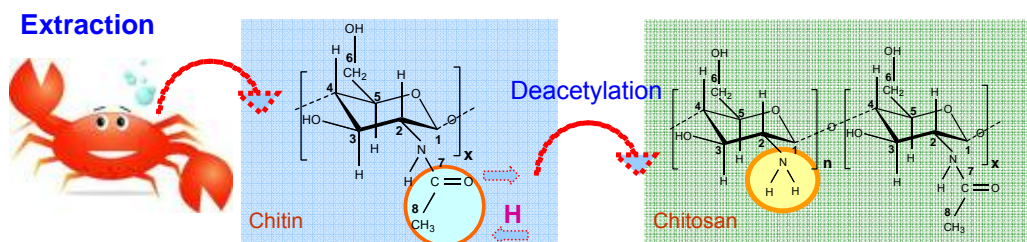


Figure 1-1. Schematic representation of both extraction and deacetylation of chitin.

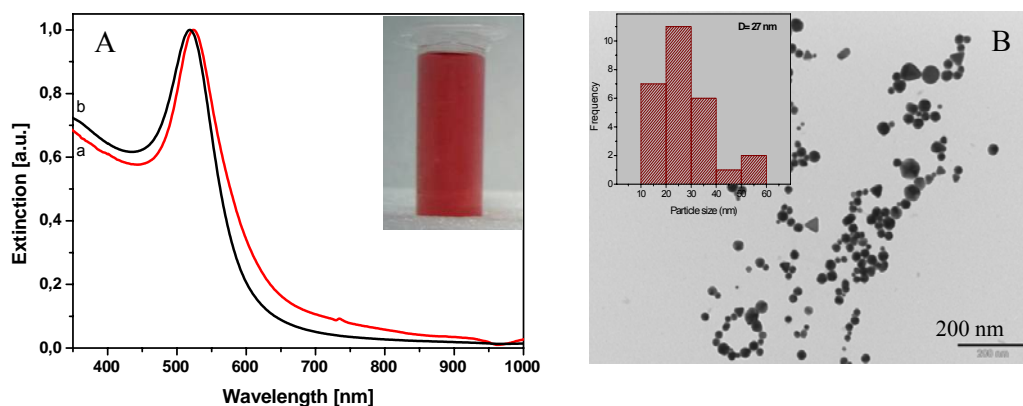
The unique properties of chitosan make it attractive for many biological applications, including controlled drug release, antibacterial agent, wound healing, nutrition supplements, removal of toxins, scaffolds for tissue engineering, semipermeable membranes, etc. [11].

## Chapter 2

# Gold-Chitosan Nanocomposites: Synthesis and Characterization

## 2.1. Gold nanoparticles formation in chitosan solution

The gold colloidal suspension was prepared at 50 °C by an environmentally friendly synthesis procedure that uses chitosan biopolymer as reducing and stabilizing agent [12]. The successful synthesis of gold nanoparticles (GNPs) was first revealed by the specific red color that the colloidal solution displays. The visible color is a result of resonant light interaction with GNPs *via* excitation of surface plasmons with contribution from light scattering and absorption. As the optical spectrum of GNPs is strongly dependent on their size and shape as well as on their local environment and electromagnetic coupling, the production of GNPs was monitored not only by eye but, more precisely, by UV-vis extinction spectroscopy and subsequent electron transmission microscopy (TEM) analysis.



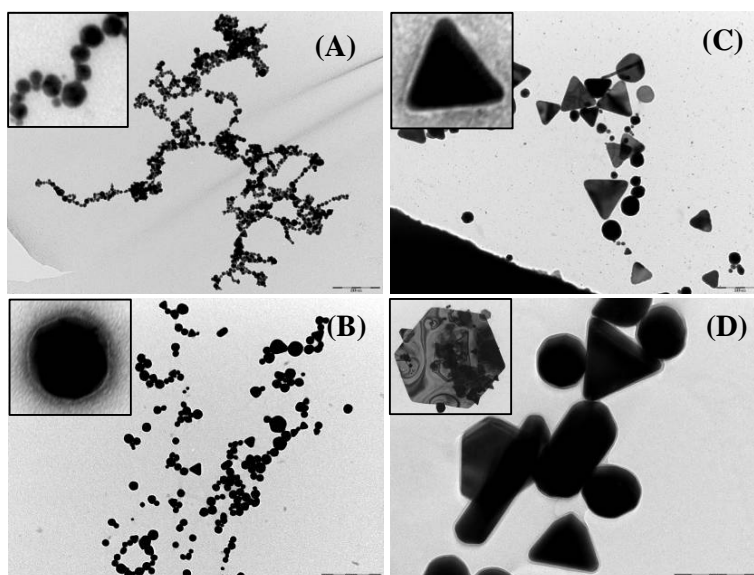
**Figure 1-2.** (A) Normalized UV-vis extinction spectra of gold nanoparticles synthesized by: (a) chitosan reduction and stabilization and (b) trisodium citrate-assisted reduction and stabilization. The inset shows a photographic image of colloidal GNPs synthesized in the presence of chitosan. (B) A representative TEM image of GNPs as prepared. The inset shows the histogram for the GNPs size distribution.

Figure 1A-2 shows a photographic image of resulted colloidal solution together with its corresponding UV-vis extinction spectrum collected at the end of reaction. The spectrum exhibits a sharp peak centered at 525 nm. For comparison, the UV-vis extinction spectrum of spherical gold nanoparticles of 18 nm diameter synthesized following the Turkevich-Frens method is also presented in Figure 1Ab-2 [13].

More precise information about the shape and size distribution of as prepared nanoparticles was obtained from TEM measurements. Figure 1B-2 shows a representative TEM picture of as synthesized gold nanoparticles. A careful analysis of the TEM images reveals that the product as prepared is mainly composed of spherical gold nanoparticles dispersed in solution with the mean particle diameter of 27 nm (see histogram in Figure 1B-2 inset). The results were obtained by analyzing several TEM images.

## 2.2. Study of gold nanoparticle formation in chitosan solution at different reaction temperatures

The effect of varying the temperature of synthesis while keeping constant the ratio between reactants is drastic and the first illustration clearly appears in Figure 2-2, where for comparison we included the TEM picture of sample prepared at 50 °C.



**Figure 2-2.** TEM pictures of GNPs as prepared. (A) 100 °C. The inset shows a close view of GNPs chain. (B) 50 °C. The inset shows a chitosan shell wrapping a single gold spherical nanoparticle. (C) 10 °C. The inset shows a chitosan layer at the edge of single gold nanocrystal. (D) 4 °C. The inset shows the magnification image of a single crystal. In panel (B) and (C) the polymer layer appears by contrast staining.

For example, in the case of sample prepared at 100 °C , Figure 2A-2 reveals the formation of spherical GNPs of  $18 \pm 2$  nm average diameter and their assembling in branched chains of tens to hundred of particles. At mild temperature, Figure 2B-2 reveals the formation of larger spherical GNPs of  $27 \pm 5$  nm average diameter. In contrast, at low temperature the Picture 2C-2 shows the formation of large anisotropic nanosheets of triangular, truncated-triangular or hexagonal shape of

lateral size from 40 nm to 200 nm, together with a few nearly spherical GNPs. Moreover, upon further decreasing the synthesis temperature from 10 °C to 4 °C, the amount of anisotropic nanosheets increased as well as their lateral size to about 300 nm for triangular nanosheets and 174 nm for hexagonal shapes (Figure 2D-2).

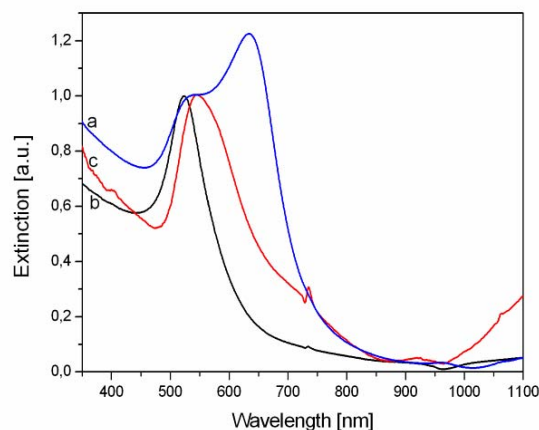


**Figure 3-2.** UV-vis extinction spectra of GNPs synthesized in chitosan solution at three representative temperatures. (a) high temperature (100 °C). (b) mild temperature (50 °C). (c) low temperature (10 °C). For a better comparison the spectra were normalized at the maximum extinction of individual GNPs.

The effect of reaction temperature on the size, shape and morphology of as synthesized GNPs was examined by UV-vis extinction spectroscopy as well. The representative sample for mild temperature synthesis (50 °C) exhibits the typical signature of surface plasmon resonance of GNPs of spherical shape (Figure 3b-2), while the representative sample for low temperature synthesis (10 °C) exhibits a significantly different corresponding spectrum (Figure 3c-2). The first plasmon resonant band appears shifted at 544 nm and, in addition to this band, a new band is evident in the near-infrared (NIR) region, the maximum beyond the range of measurement of our instrument (Figure 3c-2). This second band is consistent with a plasmonic resonance supported by anisotropic GNPs of triangular shape, as presented in TEM image (Figure 2C-2) [14]. Beside to the reminiscent band assigned to individual spherical nanoparticles, the spectrum of final solution prepared at 100 °C exhibits a second band at 634 nm which surpasses in intensity the first band (Figure 3a-2). Based on our subsequent theoretical simulations (FDTD) the band at 528 nm in the experimental spectrum of sample prepared at 100 °C may result from overlapping of the plasmon resonances of individual spherical nanoparticles with traverse surface plasmon band of *interconnected* GNPs. The second band at 634 nm can be assigned to a specific red-shifted plasmonic response given by *interconnected* GNPs as can be seen in Figure 2A-2.

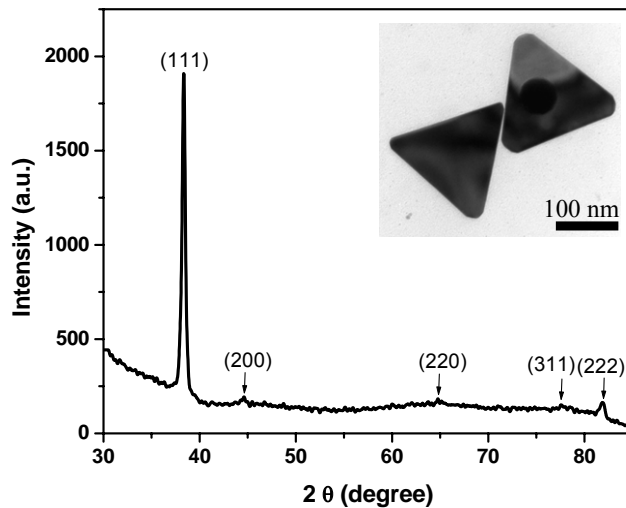


**Figure 4-2.** XRD spectrum of a representative film of composite GNPs-chitosan synthesized at 10 °C. The inset shows the magnification TEM image of sample prepared at 10 °C.

The X-ray diffraction (XRD) spectrum in [Figure 4-2](#) provides clear evidence for the crystalline structure of GNPs prepared at low temperature. All peaks for crystalline GNPs can be assigned to diffraction maxima from the {111}, {200}, {220}, {311}, and {222} planes of face-centered-cubic (fcc) gold crystal (JCPDS-file no.040784). However, a very strong intensity diffraction peak located at  $2\theta = 38.2^\circ$  ascribed to the {111} facets of fcc gold crystal, which is different from the relative intensities collected in the case of bulk crystal structure, confirms that the growing process at low temperature is highly directional, the nanosheets are mainly dominated by {111} facets and preferentially orientated parallel to the supporting surface.

### 2.3. Study of the stability of as prepared gold-chitosan nanocomposites

The interactions between gold and chitosan were investigated by Fourier transform infrared FT-IR measurements. The results prove the involvement of hydroxyl and primary amino groups in chitosan in the process of gold nanoparticles reduction and stabilization. The obtained nanoparticles show high stability under a wide range of environmental conditions, such as storage time, salt concentration and different pH.

## Chapter 3

# Chitosan-Mediated Synthesis of Anisotropic Silver Nanoparticles

### 3.1. The growth of triangular nanoplates

#### 3.1.1. First step: Preparation of seeds solution

To synthesize silver nanoparticles of controllable size and shape, we have developed a seed-mediated growth approach [15]. A stock aqueous solution of silver particles called “seeds” was prepared by the reduction reaction of silver nitrate with sodium borohydride at ice temperature.

#### 3.1.2. Second step: The growth of triangular silver nanoplates

In the second step, aqueous solutions of seeds, trisodium citrate (TSC), ascorbic acid and chitosan were combined and thermostated at  $35 \pm 2$  °C. To this mixture, silver nitrate was added dropwise under continuous magnetic stirring. The reaction was completed within a total of 5 minutes during which time the color of solution changes from colorless to yellow, then orange, pink, mauve, blue, turquoise and finally to dark green.

#### 3.1.3. Morphology analysis by TEM

Detailed characterization of the silver nanoparticles morphology was obtained by transmission electron microscopy (TEM) measurements.

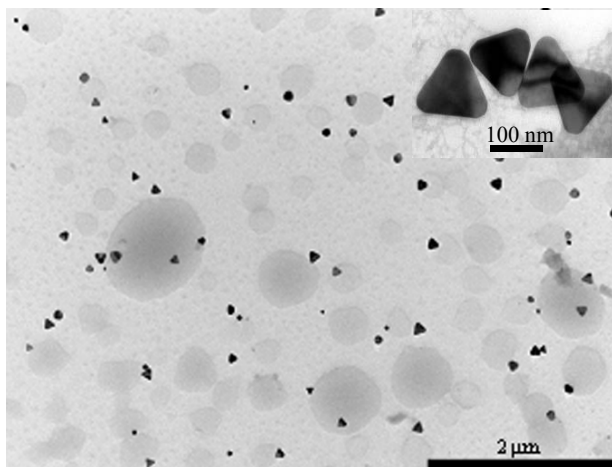


**Figure 1-3.** Representative TEM image of as prepared triangular silver nanoplates. The inset shows a close view of silver nanotriangles.

Figure 1-3 illustrates a representative TEM picture of obtained silver nanostructures which clearly reveals the formation of individual silver particles mainly of triangular and truncated-triangular shape with edge lengths from 115 to 123 nm. The results were obtained by analyzing several TEM images.

### 3.1.4. Surface plasmon resonances of triangular silver nanoplates

The optical properties of as prepared triangular silver nanoplates were investigated by UV-VIS-NIR extinction measurements at the end of reaction. The spectrum of the colloidal suspension (Figure 2a-3) exhibits all four characteristic peaks corresponding to different modes of plasmon excitation of triangular nanoplates [16].

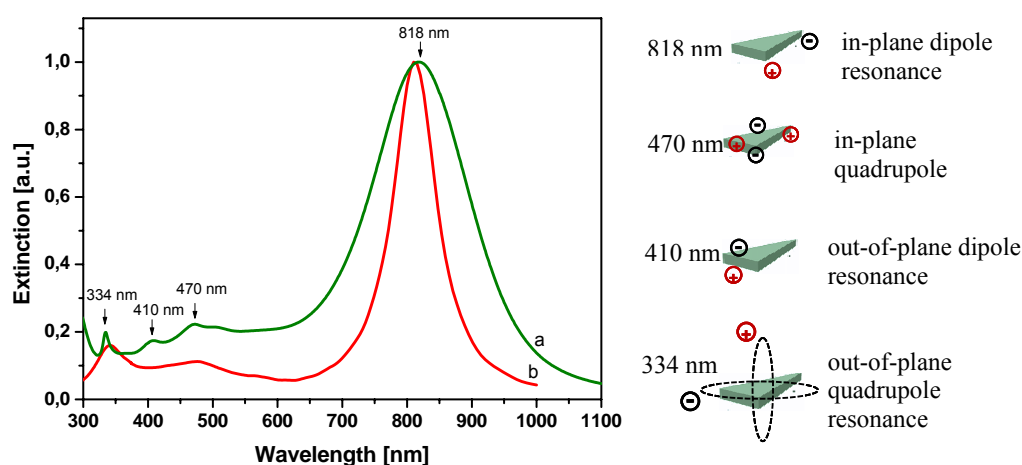


Figure 2-3. Comparison of (a) measured and (b) FDTD calculated extinction spectra corresponding to as prepared silver triangular nanoplates.

The dominant two bands, namely the intense and broad one situated at 818 nm and the sharp band located at around 334 nm, are attributed to the in-plane dipole resonance and the out-of-plane quadrupole resonance, respectively. The weak band at 410 nm is due to the out-of-plane dipole resonance and the band at 470 nm is attributed to the in-plane quadrupole resonance. The calculated extinction spectrum in Figure 2b-3 (finite difference time domain – FDTD – numerical simulations) shows a nice agreement with the experimental optical spectrum in Figure 2a-3 and confirms the spectral response of isolated silver nanoplates in UV–Vis–NIR domain.

## 3.2. Tuning the size and morphology of silver nanoparticles

### 3.2.1. The effect of trisodium citrate on the nanoparticle size and morphology

To get insight into the silver nanoparticles formation, we investigate the relative effect of several reaction compounds, including TSC, chitosan and ascorbic acid concentration. The effect of varying the TSC concentration while keeping the other experimental condition constant is drastic and the first illustration appears clearly in [Figure 3-3](#).

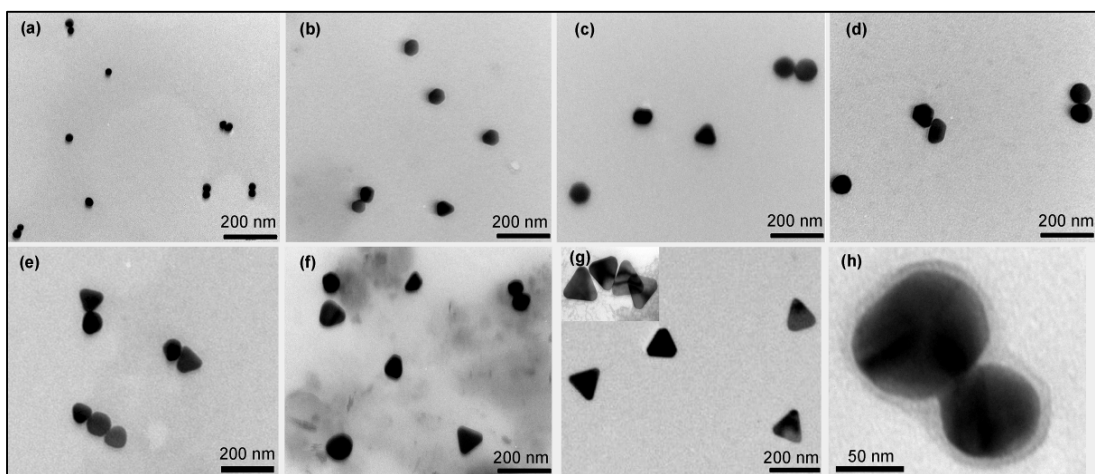


**Figure 3-3.** TEM pictures of as prepared silver colloids by increasing the TSC concentration (from (a) to (g)). (h) A closer view of silver nanoparticles coated by a chitosan layer.

TEM pictures in [Figure 3-3](#) clearly show that the nanoparticles evolve from the initial spherical to triangular shape, depending on TSC concentration. It is clear that high TSC concentration resulted in the formation of large anisotropic nanoplates, mainly of triangular and truncated-triangular shape together with a few nearly spherical silver nanoparticles. Silver nanoplates were not obtained with low citrate concentration and spherical particles were the main product, even after prolonging the time of synthesis ([Figure 3a-3](#)). In [Figure 3h-3](#) a closer view of silver nanoparticles recorded by staining contrast method clearly reveals the presence of thin chitosan layer around the particles.

The effect of different reaction parameters on the size, shape and morphology of obtained nanoparticles was investigated by UV-VIS-NIR extinction spectroscopy as well. [Figure 4-3](#) shows the UV-VIS-NIR extinction spectra from these seven samples resulted at the end of reaction, together with their color pictures. The samples display a progression of color changes as the main LSPR peak is increasingly red-shifted from 414 nm to 818 nm.

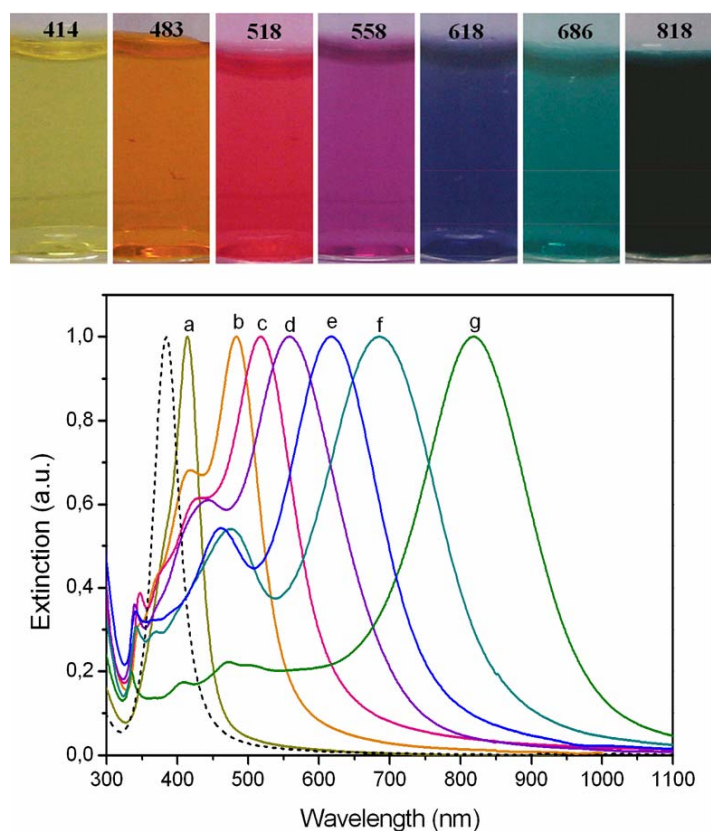
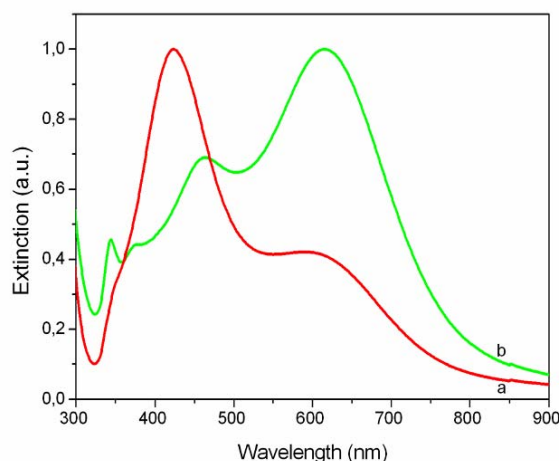


**Figure 4-3.** Normalized UV-VIS-NIR extinction spectra and corresponding photographs of as-prepared silver colloids by increasing the TSC concentration (from (a) to (g)). The numbers on labeled vials correspond to the spectral position of the in-plane dipole resonance band. For comparison, we inserted the extinction spectrum of seeds solution (dashed curve).

The yellow colloidal solution exhibits a single extinction peak, slightly asymmetric, located at 414 nm which can be assigned to the resonance mode of spherical silver nanoparticles [17]. We notice that this solution outcomes from the growth process conducted with the lowest sodium citrate concentration. At the opposite side, the dark-green colloidal solution exhibits four extinction peaks and outcomes from the growth process conducted at highest sodium citrate concentration. The spectra from other samples prepared with intermediate sodium citrate concentration reveals similar features. However, in relation to the spectral positions of triangular nanoplates discussed above, the corresponding bands are spectrally shifted, specifically to blue for the in-plane dipole resonance due to the decrease of edge length and to red for the out-of-plane quadrupolar resonance due to the increase of nanoplates thickness. The optical extinction measured in between two lateral bands is slightly higher than would be expected from samples of pure triangular nanoplates. The result can be explained by the overlapping between the specific bands of nanoplates and the plasmon resonances of spherical silver nanoparticles, which grow in the detriment of triangular nanoplates when the concentration of TSC is low.

### 3.2.2. The effect of chitosan concentration on the nanoparticle size and morphology

To infer the role of chitosan, two comparative experiments were carried out: (a) in the absence of chitosan in solution and (b) in the presence of chitosan.



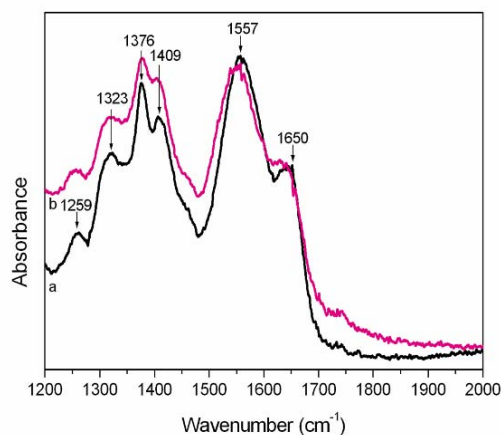
**Fig. 5-3.** Normalized UV-VIS-NIR spectra of obtained samples: (a) without chitosan. (b) with 2 mg/mL chitosan concentration

Figure 5-3 shows the extinction spectra recorded from the two final solutions. The analysis reveals that in the first case the spectrum (Figure 5a-3) is consistent with the formation of spherical nanoparticles (dominant extinction at 423 nm) while in the second case the spectrum (Figure 5b-3) is consistent with the formation of triangular particles as the quadrupole plasmon mode at 340 nm and the dipolar band at 618 nm are visible. However, pure nanoplates are obtained uniquely in the presence of chitosan and high concentration TSC, clearly indicating that the two compounds act synergistically in the anisotropic growth.

## 3.3. Stability of as prepared chitosan-silver nanocomposites

### 3.3.1. FT-IR characterization

The Fourier transform infrared (FT-IR) measurements were used to analyze the nanocomposites structure and identify the molecular groups in interaction with silver nanoparticles. Figure 6-3 shows the two representative FT-IR spectra featuring the main vibrational bands of chitosan according to spectroscopic data in literature. [18].



**Figure 6-3.** FT-IR spectra of: (a) pure chitosan film. (b) a typical chitosan-silver nanocomposites film.

Most of chitosan characteristic bands at  $1650\text{ cm}^{-1}$  (amide I band characteristic to C=O stretching of N-acetyl group),  $1409\text{ cm}^{-1}$  (bending vibration of OH group),  $1376\text{ cm}^{-1}$  (symmetric deformation vibration mode of  $\text{CH}_3$ ),  $1323\text{ cm}^{-1}$  ( $\text{CH}_2$  wagging vibration mode in primary alcohol) and  $1259\text{ cm}^{-1}$  (the amide III vibration mode due to combination of N-H deformation and C-N stretching) are insensitive to the presence of metal surface. However the most prominent band at  $1557\text{ cm}^{-1}$  assigned to amino group in pure chitosan film shifts to a lower wavenumber ( $1548\text{ cm}^{-1}$ ) in the presence of silver nanoparticles. The result clearly identifies the involvement of primary amino groups in interaction with metal surface, the amino groups acting here as capping sites for the silver nanoparticles stabilization.

### ***3.3.2. Study of the chitosan-silver nanocomposites stability under a wide range of environmental conditions***

Besides the size and shape control, the performance of silver nanoparticles in different applications strongly depends on their chemical stability under a wide range of environmental condition, such as storage time, salt concentration, different pH, biological fluids, etc.

Generally, the stability of colloidal systems refers to their tendency to aggregate or to their tendency to sediment under the action of gravity. The stability of anisotropic nanoparticles in solution should be also treated in terms of their size and shape evolution (etching) in different physical and chemical conditions including storage time, pH, biological media etc. Herein, we investigated the stability of as-synthesized chitosan- silver nanocomposites towards aggregation and their size and shape conservation in various environmental conditions. The results showed that the adsorbed biopolymeric chain provides an electrosteric barrier to nanoparticles that keeps them segregated in solution under a wide range of environmental conditions, such as storage time, salt concentration, different pH and cellular medium.

## Chapter 4

# Chitosan-Coated Anisotropic Silver Nanoparticles as Versatile LSPR-SERS Plasmonic Sensors

## 4.1. Chitosan-coated anisotropic silver nanoparticles as dual LSPR- SERS plasmonic sensors in solution

### 4.1.1. LSPR bulk refractive index (RI) sensitivity

Different water/glycerol mixtures were prepared with the aim to gradually tune the *effective* (bulk) refractive index of the nanoparticle environment from 1.333 (pure water) to 1.473 (pure glycerol).

The chitosan-coated silver nanoparticles were separated from the original solution by centrifugation and re-dispersed in the above water-glycerol solutions. Figure 1A-4 illustrates the normalized UV-VIS-NIR extinction spectra collected from eight samples suspended in water-glycerol mixtures. The similarity of extinction spectrum recorded before and after the transfer to water-glycerol mixtures clearly confirms the high stability of silver nanoparticles. Notably, the presence of chitosan around the particle did not impact negatively the exchange with the surrounding medium and liquid can come in contact with the nanoparticle surface, keeping the ability of particles to sense the modification of RI values.

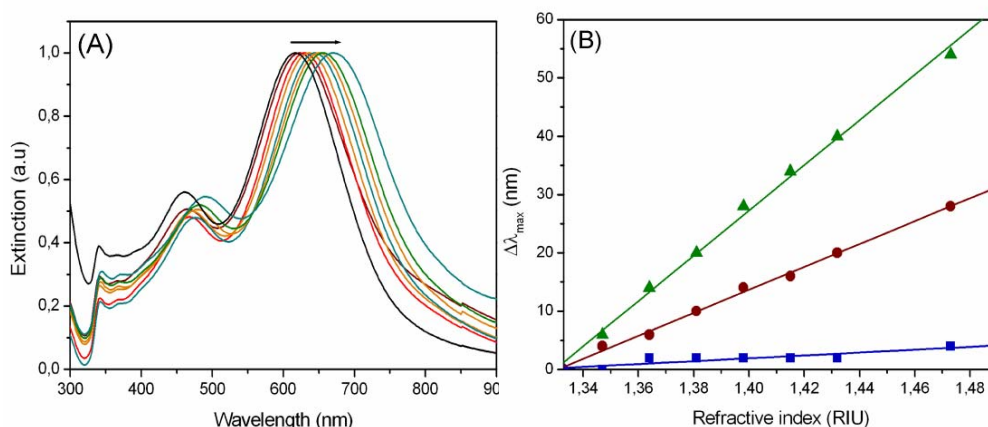


**Figure 1-4.** (A) Normalized UV-VIS-NIR extinction spectra of silver colloid suspended in aqueous solutions of glycerol of various refractive indices, from left to right: 1.333, 1.347, 1.364, 1.381, 1.398, 1.415, 1.432, and 1.473. All spectral intensities were normalized with respect to those of the in-plane dipolar plasmonic band. (B) Plot depicting the linear dependence of the plasmonic bands position on the refractive index: (▲) in-plane dipolar plasmonic band, (●) combination of the in-plane quadrupolar band and out-of-plane dipolar mode, and (■) out-of-plane quadrupolar band.

The localized surface plasmon resonances (LSPR) sensitivity of chitosan-coated silver nanoparticles to bulk refractive index (RI) of solutions was evaluated by plotting the shift of the plasmonic bands wavelength position ( $\Delta\lambda_{\text{max}}$ ) against the refractive index (Figure 1B-4). The plasmonic resonances were found to linearly red shift as the solvent refractive index was increased. The linear regression analysis yielded a bulk refractive index sensitivity of 387 nm RIU<sup>-1</sup> for the in-plane dipolar plasmonic band, 196 nm RIU<sup>-1</sup> for combination between the in-plane quadrupolar mode and out-of-plane dipolar mode and 25 nm RIU<sup>-1</sup> for the out-of-plane quadrupolar peak, respectively.

#### *4.1.2. LSPR surface sensitivity*

The LSPR approach to detect the presence of biomolecular analytes was previously demonstrated for an ensemble of nanoparticles immobilized on a transparent substrate and, subsequently, extended to the limit of single nanoparticles [19]. In our case, we used anisotropic silver nanoparticles enveloped in chitosan nanoshells as a potential LSPR chemosensor in solution and p-ATP as the target analyte. In comparison to other molecules, thiols interact very strongly with silver surface because they may form strong covalent bonds to the surface silver atoms through back  $\pi$ -bonding from the sulfur bonds. Figure 2A-4, part a, illustrates the extinction spectrum of p-ATP mixed colloidal silver nanoparticles (final p-ATP concentration of  $9.9 \times 10^{-6}$  M) recorded several hours after adding the analyte to colloidal solutions in order to achieve the maximum chemisorptions of the p-ATP molecules. For comparison, Figure 2A-4, part b, shows the reference spectrum recorded from blank solution (without p-ATP). However, compared with the original spectrum of silver–chitosan nanocomposites, a decrease in the intensity of the in-plane dipolar plasmonic band with a concomitant red shift of 10 nm was observed in the presence of p-ATP molecules. In addition, the absorption maximum of the other bands experiences a shorter shift than that of the longitudinal band (6 nm for the out-of-plane dipolar mode and 2 nm for the out-of-plane quadrupolar band). This finding is consistent with the results above which demonstrate the higher sensitivity of the in-plane dipole resonance band toward the chemical environment of these nanocomposites.

The presence of the analyte molecules on the silver surface leads to a change of the electrical charge on the nanoparticles surface as well as a modification of the refractive index of the medium surrounding the particles which consequently induces a decrease of the extinction band intensity and their shifts to longer wavelengths, respectively. The data show that chitosan acts as an excellent protective shell against aggregation and allows the analyte molecules to diffuse through its internal nanoporosities and to attach on the metal surface, which is relevant for investigation in real biological media.

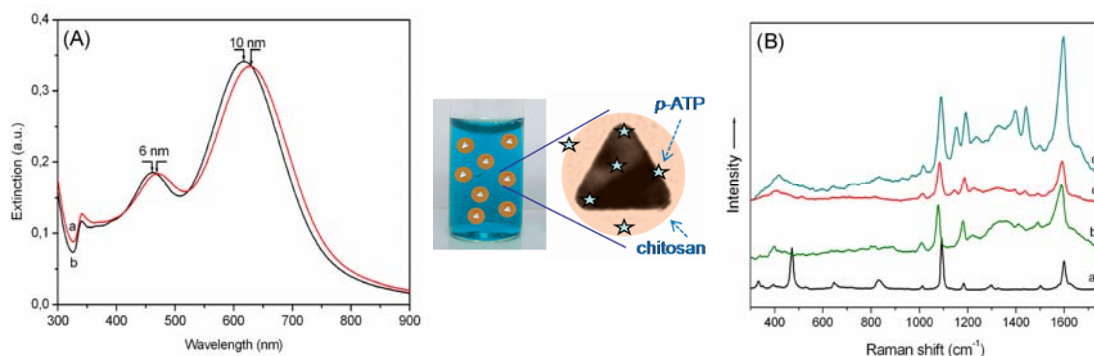


**Figure 2-4.** (A) UV-VIS-NIR extinction spectra of silver colloid: (a) after adding *p*-ATP solution, (b) before adding *p*-ATP solution (B) The normal Raman spectrum of solid *p*-ATP (a) and SERS spectra of *p*-ATP recorded by laser excitation wavelength 785 nm (b), 633 nm (c), 532 nm (d). For SERS measurements the concentration of *p*-ATP molecules in the sample solution is  $9.9 \times 10^{-6}$  M.

#### 4.1.3. SERS sensitivity

Next we demonstrated the detection and identification of adsorbed target molecules by surface enhanced Raman spectroscopy (SERS) measurements, which provide both molecular specificity and higher sensitivity than LSPR measurements. High-quality SERS spectra were recorded with three laser excitation lines from visible (532 nm and 633 nm) and near infrared (NIR) (785 nm), as shown in Figure 2B-4. The following analysis of the enhancement of specific vibrational bands clearly identifies both the presence and orientation of *p*-ATP molecule on the silver surface. The strong bands at 1093 and 1596  $\text{cm}^{-1}$  together with other two medium intense bands at 465 and 1171  $\text{cm}^{-1}$  are assigned to  $a_1$  vibrational modes of *p*-ATP, namely C-S stretching vibration, C-C stretching mode, C-C-C bending vibration and C-H bending mode, according to literature [20]. The strong enhancement of the C-S stretching vibration and the lack of S-H stretching mode at 2558  $\text{cm}^{-1}$  clearly suggest the rupture of S-H bond and the attachment of *p*-ATP to the silver surface through its sulfur atom.

An interesting feature is that no SERS signal appears from the chitosan biopolymer. Similar behavior has been previously reported in literature for other polymers used to stabilize metal nanoparticles employed as SERS-active tags or biocompatible SERS substrates [21].

As a proof of concept for biosensing applications and dual functionality of plasmonic platform we demonstrated the detection of a relevant biological molecule, adenine, through the combined LSPR and SERS measurements. We found that the lowest detectable concentration of adenine adsorbed on chitosan coated anisotropic silver colloidal nanoparticles was  $12 \times 10^{-6}$  M.

## 4.2. Chitosan-coated anisotropic silver nanoparticles for SERS detection at single molecule level

In the following we are interested to push the SERS detection limit towards single molecule level. In view of this aim the occurrence of *hot-spots*, such as gaps and junctions created between interconnected nanoparticles are obviously needed. We demonstrated previously that the aggregation agent could not induce nanoparticles aggregation. Therefore, the assembling of 2-3 anisotropic nanoparticles after solvent evaporation on a solid substrate could create *hot-spots* between nanoparticles. For this purpose, a simple drop coating method was used to deposit thin films consisting on chitosan-silver nanoparticles previously mixed with the analyte molecules [22]. This procedure gives rise to small clusters of anisotropic silver nanoparticles with narrow intraparticle spaces which can generate giant Raman enhancement of the molecules located in these regions. Figure 3-4 schematizes the procedure of preparation of both anisotropic silver nanoparticles and SERS substrates.

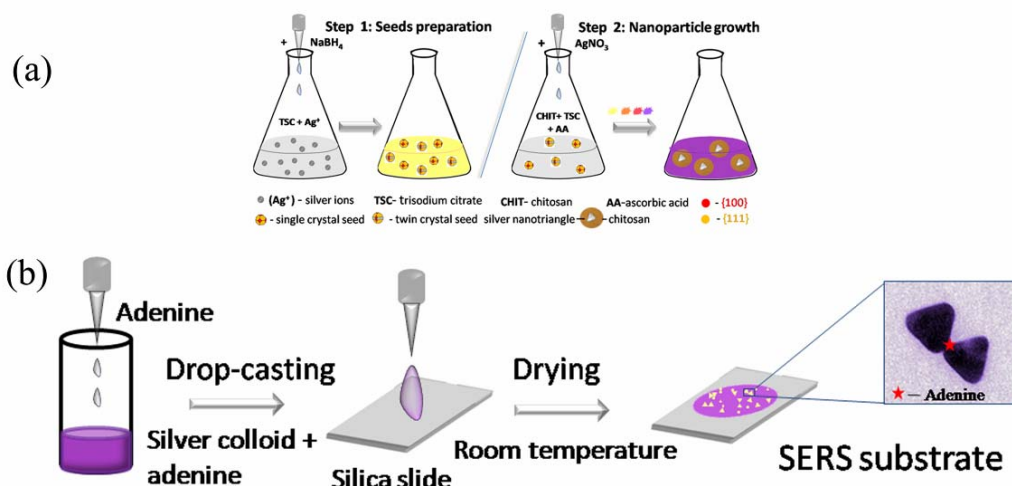
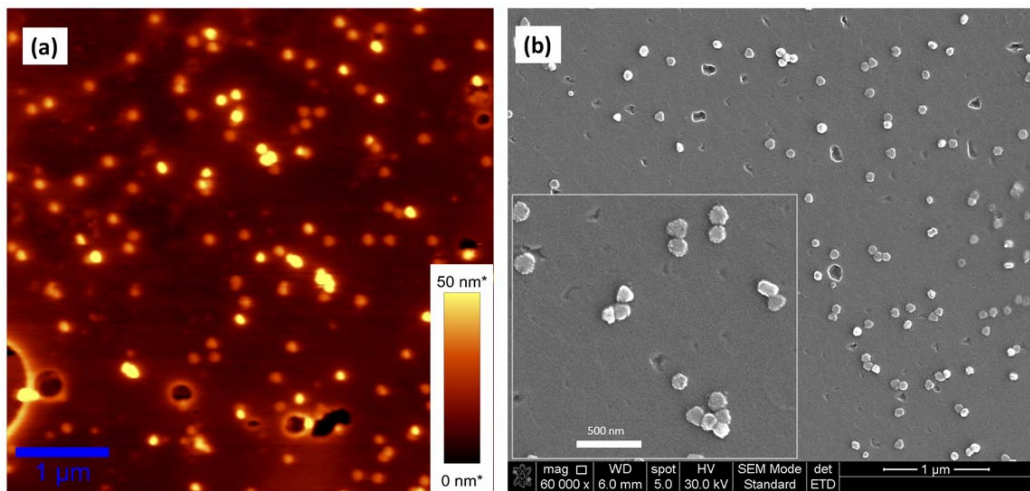


Figure 3-4. Schematic illustration of (a) a typical two-step procedure for the growth of chitosan-coated anisotropic silver nanoparticles and (b) the solid-film preparation.

### 4.2.1. Morphological and optical characterization of SERS substrates

Detailed characterizations of the films morphology were obtained by both atomic force microscopy (AFM) and scanning electron microscopy (SEM) imaging. As one can see from Figure 4-4 the AFM and SEM images prove the presence of isolated silver nanoparticles, as well as small clusters formed on the solid substrate surface.



**Figure 4-4.** (a) AFM image of a representative SERS active film. The scale bar is 1  $\mu\text{m}$ . (b) Representative SEM image of the SERS active film. The inset shows a closer view of the small clusters formed on the solid film.

The optical properties of as prepared films were investigated by UV-VIS-NIR measurements. [Figure 5-4](#) shows the UV-VIS-NIR extinction spectra of the colloidal solution and the SERS substrate. As compared to the spectrum of colloidal silver-chitosan nanocomposites ([Figure 5b-4](#)), the plasmon resonant bands of the solid film appear red shifted by approximately 7 nm, slightly broadened and their intensity significantly decreased. The shift and the slight broadening of the bands could be consistent with the formation of dimers, trimers or more complicated, but small, clusters on the silica slide surface as can be observed in SEM images ([Figure 4b-4](#)).

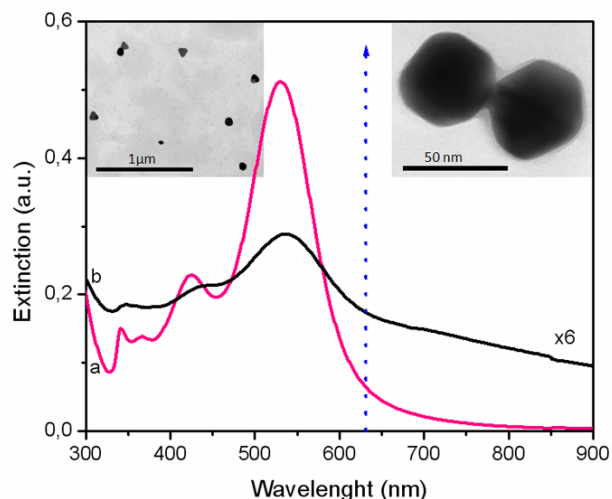


**Figure 5-4.** UV-VIS-NIR extinction spectra of (a) silver colloidal nanoparticles in the growth medium and (b) the film prepared with  $12 \times 10^{-12}$  M adenine concentration. The arrow indicates the position of laser excitation line. The left inset shows a representative TEM picture of as prepared silver nanoparticles. The right inset shows a dimer of anisotropic silver nanoparticles embedded in chitosan matrix.

#### 4.2.2. Ensemble-averaged SERS of adenine

To assess the SERS activity of as prepared substrates we firstly performed the measurements on the sample containing the highest adenine concentration ( $12 \times 10^{-6}$  M final concentration). Figure 6a-4 part (a) shows the SERS spectrum of adenine recorded with 632.8 nm excitation wavelength. For comparison, the Raman spectrum of the solid sample is also shown in Figure 6a-4 part (b). The illustrated spectrum in Figure 6a (a)-4 clearly identifies the presence of analyte molecules on the silver surface and allows addressing the adenine orientation by analyzing the enhancement of specific band vibrations. The typical and most prominent bands at 737 and 1331  $\text{cm}^{-1}$  observed in the SERS spectrum correspond to those present at 722  $\text{cm}^{-1}$  (ring breath whole molecule) and 1333  $\text{cm}^{-1}$  (str C5-N7, N1-C2, bend C2-H, C8-H) in the Raman spectrum of adenine [23].

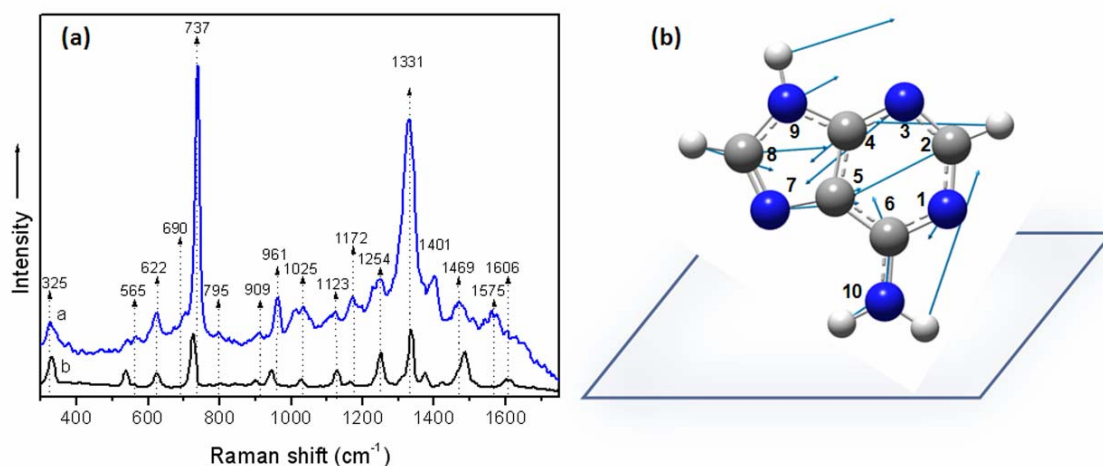


**Figure 6-4.** (a) The SERS spectrum of adenine on solid film (a). The normal Raman spectrum of solid adenine (b). For SERS measurements the concentration of adenine molecules in the samples is  $12 \times 10^{-6}$  M. (b) The schematic drawing of the adenine molecule orientation relative to the silver surface.

The analysis of the SERS fingerprint indicates that the interaction with the silver surface takes place via amino groups and the adenine molecules adopt a tilted orientation relative to the metal surface, as illustrated in Figure 6b-4.

Observing only highly populated SERS substrates can hide the presence of *hot-spots* and dynamic behavior of probe molecules that are important to characterize SERS experiments. Therefore, we proceed to reduce the concentration of the probe molecule. We found that the films containing lower adenine concentrations revealed the same features, excepting that the SERS intensity progressively decreased. Moreover, the spectra collected from the film with the lowest

adenine concentration were characterized by strong temporal fluctuations of some peak intensities and peak/peak intensity ratios.

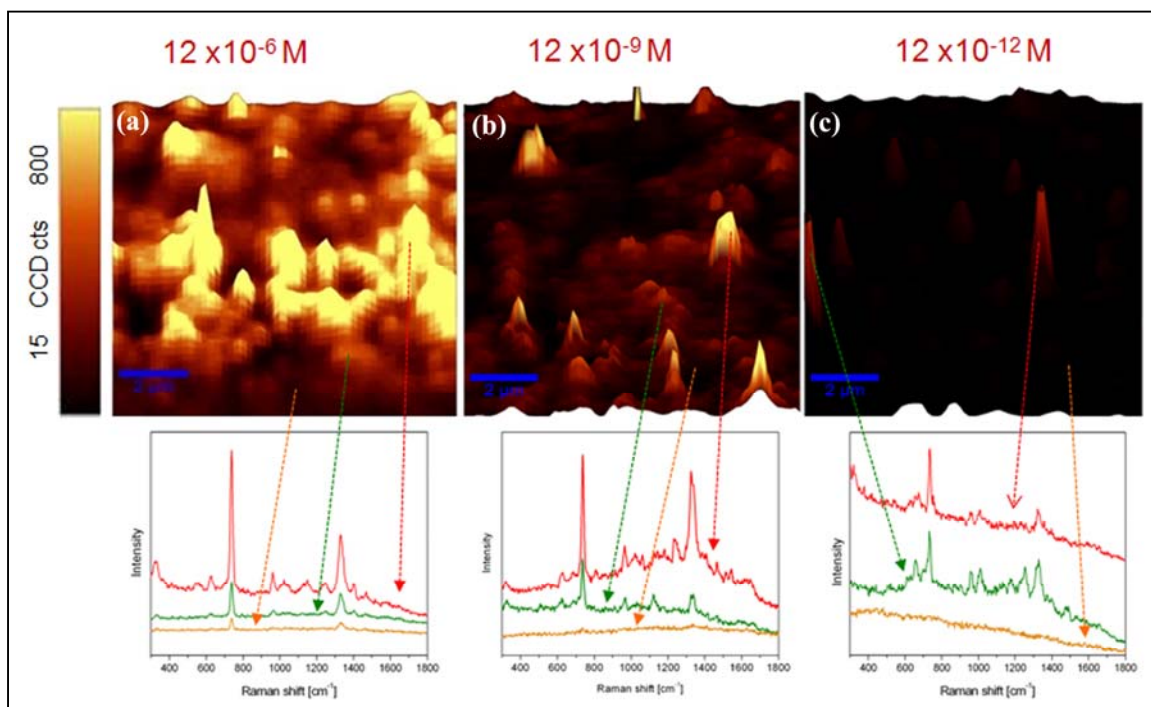


**Figure 7-4.** Top: The 3D SERS spatial maps obtained by plotting the distribution of  $737 \text{ cm}^{-1}$  vibrational mode intensity over the scanned surfaces of films containing different adenine concentration (a)  $12 \times 10^{-6} \text{ M}$ , (b)  $12 \times 10^{-9} \text{ M}$ , (c)  $12 \times 10^{-12} \text{ M}$ . Down: Selected SERS spectra of adenine collected on different points onto the maps presented top. The map in C shows that adenine can be detected at single molecules regime. The scale bar is  $2 \mu\text{m}$ .

Additional information about the enhancement performances of these sensing platforms was provided by performing scanning SERS imaging on the SERS substrates.

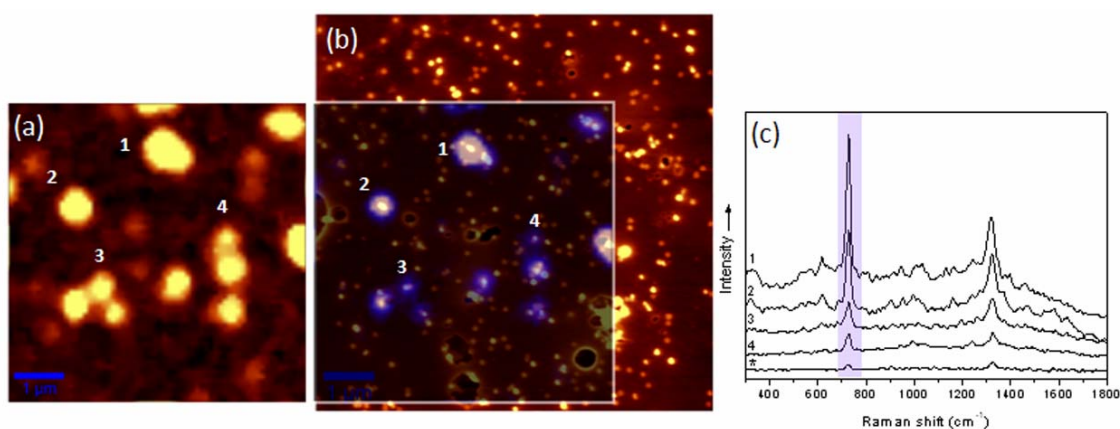


**Figure 8-4.** Correlation between the SERS map and the surface distribution of nanoparticles as recorded by AFM: (a) unprocessed SERS map corresponding to the processed map presented in (b). (b) processed (made transparent) SERS map of adenine  $737 \text{ cm}^{-1}$  band superposed over the AFM image. Note that the area scanned by AFM tip is larger than area scanned by the laser spot. The scale bar is  $1 \mu\text{m}$ . (c) Example of selected SERS spectra as collected from the spots indicated in (a) and (b). The spectrum marked by \* was collected from the substrate outside of nanoparticle ensembles.

Figure 7-4 presents SERS images obtained by plotting the intensity of the SERS band at  $737\text{ cm}^{-1}$  over the scanned area of films containing different adenine concentrations, as indicated, together with the SERS spectra selected from various substrate locations revealing different enhancement levels. Thus, Figure 7a-4 shows a representative SERS image collected from the film with  $12 \times 10^{-6}$  M adenine concentration. Although an irregular distribution of SERS intensity over the selected surface is observed, it is important to notice that valuable SERS spectra were recorded over the whole scanned area. As expected, by gradually diminishing the adenine concentration the overall intensity of the SERS bands is decreasing (see Figure 7b-4).

To further investigate the origin of the most intense SERS spots we correlated the films morphology with its SERS efficacy. Figure 8b-4 illustrates a correlated AFM-Raman image obtained by overlaying the SERS spatial map over the AFM scan of the same area. The existence of very high SERS enhancement zones coincides with assemblies of particles such as dimers, trimers or more complex clusters. Figure 8c-4 shows a selection of SERS spectra corresponding to the spots indicated by numbers 1-4 in Figure 8-4 parts a and b. It is demonstrated that the coupled nanoparticles could create *hot-spots* of very high electromagnetic field enhancement, which can promote a tremendous increase in the Raman intensity making possible to detect SERS signal even from single molecules [24]. It is expected that, during the solvent evaporation, the analyte molecules are bound not only on the surface of the nanoparticles but also are trapped on sites located in gaps and junction created between neighboring nanoparticles. Therefore, the highest Raman enhancement is promoted by such *hot-spots* which densities vary onto the film surface (see Figure 8-4).

#### 4.2.3. Single-molecule SERS of adenine

Our interest was further focused on the film prepared with  $12 \times 10^{-12}$  M adenine concentration, since the detection of such ultra-low concentration could be considered as evidence for single molecule sensitivity. Figure 7c-4 illustrates a representative SERS image of the  $737\text{ cm}^{-1}$  vibrational mode collected from the film with the lowest adenine concentration. One can see that the SERS activity is highly localized corresponding to few active Raman scattering sites. The selected spectra in Figure 7c-4 down clearly reveal that these *hot-spot* locations promote a giant amplification, which makes possible to detect SERS signal even from such a low analyte concentration. On the basis of the spectral analysis a dramatic change of the SERS fingerprint was observed as function of *hot-spots* location (see Figure 9A-4). Thus, we found that some *hot-spots* promote a great Raman enhancement particularly for some weak or inactive SERS modes that were not present in spectrum recorded for high adenine concentration. Considering the surface selection rules according to that the vibrational modes that involve a large change of the polarizability

perpendicular to the metal surface are the most enhanced ones, we speculated that these spectral differences could be connected with the reorientation of analyte molecules during measurements.

The time evolution of the SERS signal of several *hot-spots* located on the substrate containing the lowest adenine concentration was also investigated by recording time series of SERS spectra. We found that the SERS signal was characterized by spectacularly temporal fluctuations of some peak intensities as well as of peak/peak intensity ratios as can be seen in [Figure 9A-4](#).

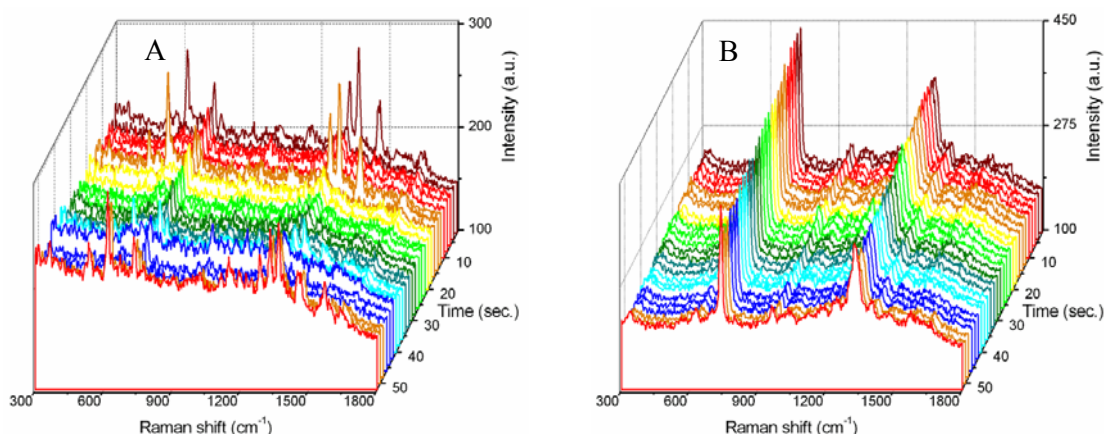


**Figure 9-4.** Waterfall-plot of time series of SERS spectra of adenine, showing the characteristic single molecule blinking. The spectra was collected from the film with the lowest adenine concentration. Waterfall plot of time series of SERS spectra of adenine collected from a hot-spot located on the film with the highest adenine concentration. The integration time was 0.5 s and the excitation line was 632.8 nm.

Notably, in our system such a variation of SERS fingerprints recorded from *hot-spots* location can be observed only on the sample with the lowest adenine concentration. By gradually increasing the adenine concentration, the overall intensity of the SERS bands is increasing, whereas the SERS spectra recorded from different films regions show similar features. [Figure 9B-4](#) illustrates selected time-series spectra collected from a *hot-spot* located on the film containing the highest adenine concentration. As one can see the spectrum is very stable in time. The reproducibility of the SERS measurements was tested by recording several individual and time-series spectra in the same way from different films regions and the difference was only between the overall intensities with no significant change of the band positions, full width of Raman bands or the peak/peak intensity ratios.

The performance of recording a SERS signal from extremely low analyte concentration, only from a few regions of the substrate surface corroborated with the signal fluctuating behavior allow us to assert that the film-entrapped chitosan coated anisotropic silver nanoparticles is a highly SERS-efficient, able to detect adenine at single molecule level.

## Chapter 5

# Synergistic Antibacterial Activity of Chitosan-Silver Nanocomposites on *Staphylococcus Aureus*

### 5.1. MIC and MBC determination

In our study we performed comparative tests to evaluate the impact of row silver nanoparticles, chitosan-silver composites and chitosan biopolymer against two representative methicillin-resistant *Staphylococcus aureus* (*S. aureus*) strains. The tests were made by incubating the bacteria in the presence of different concentration of nanoparticles and chitosan. Two supplementary samples were prepared as negative (only sterile growth medium) and positive (bacterial suspension without nanoparticles or chitosan) control. The antimicrobial effects were evaluated using the minimal inhibitory (MIC) and minimum bactericidal concentrations (MBC) which are the standard microbiological measures to evaluate the bacteriostatic and bactericidal properties of antimicrobial agents. Bacterial growth was evaluated visually and the MIC was recorded as the lowest concentration that completely inhibits growth. To evaluate the MBC, 100  $\mu$ L aliquots were taken out from the wells without visible cell growth and plated onto Mueller Hinton agar plates. Then the plates were incubated at 37°C for 24 hours. After incubation colony forming units (CFUs), corresponding to the number of surviving cells, were counted. The MBC is defined as the lowest concentration that inhibits colony formation. To certify the reproducibility of our results, all antibacterial activity tests were performed in duplicate and were repeated after several days. Results are listed in [Table 1-5](#) and represent the mean MIC and MBC values for each antibacterial agent tested. The standard deviation of MIC and MBC data was also given in [Table 1-5](#).

**Table 1-5.** MIC ( $\mu$ g/mL) and MBC ( $\mu$ g/mL) of chitosan-silver nanocomposites, silver nanoparticles and chitosan against two strains of *S. aureus*.

Strain	Chitosan-silver nanocomposites synthesized at 0 °C		Chitosan-silver nanocomposites synthesized at 35 °C (4 mM TSC)		Chitosan-silver nanocomposites synthesized at 35 °C (16.5 mM TSC)		Silver nanoparticles (without chitosan) synthesized at 0 °C		Chitosan	
	MIC	MBC	MIC	MBC	MIC	MBC	MIC	MBC	MIC	MBC
UCLA 8076	1.25 $\pm$ 0.75	6 $\pm$ 0	4 $\pm$ 0	15 $\pm$ 0	4.5 $\pm$ 1.5	19 $\pm$ 3	9 $\pm$ 4	>28	10 $\pm$ 0	30
1190	0.75 $\pm$ 0.25	6 $\pm$ 0	4 $\pm$ 0	13.5 $\pm$ 1.5	6 $\pm$ 0	22 $\pm$ 0	10.5 $\pm$ 2.5	>28	10 $\pm$ 0	30

For silver nanoparticles without chitosan MIC and MBC values are smaller than or similar to those reported previously [9]. Chitosan, when applied alone, exerts antibacterial effects at concentrations similar to those found in the literature [25]. Chitosan-coated silver nanoparticles synthesized at both

0°C and 35°C showed more pronounced effects than their components [26]. This is especially evident for their bacteriostatic action as evidenced by the MIC. The synergistic effect observed might be explained by the change of nanoparticles surface chemistry, and in consequence, their biological properties, when covered with a biopolymer.

## 5.2. AFM imaging of the antibacterial effects of silver nanoparticles on *S. aureus*

In this study we used atomic force microscopy (AFM) to investigate the morphological changes and structural damage induced in *S. aureus* cells after exposition to chitosan-silver nanoparticles. AC mode was used to acquire both the topographical and phase AFM image during the scan (see Figure 1-5).

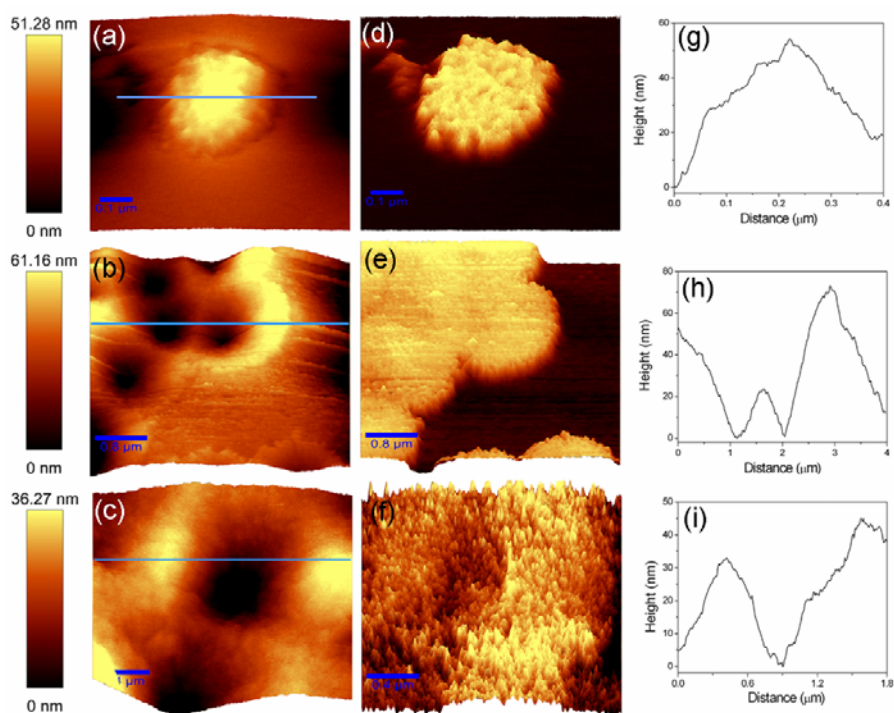


**Figure 1-5.** Representative AFM topographies of *S. aureus*: (a) without treatment, (b), (c) after treatment with chitosan-silver nanocomposites synthesized at 0 °C. Phase mode AFM images (d-f) and cross sectional analysis (g-i) of the corresponding topographies.

The topographical and the corresponding phase image (Figure 1-5 a and d) show the typical near-spherical shaped form of a single *S. aureus* cell before exposure to silver nanoparticles. In contrast, a dramatic change of the cell structure of *S. aureus* can be seen after treatment with chitosan-silver nanocomposites. The topographical AFM images in Figure 1-5 b and c clearly reveal several deep craters in biofilm structure resulting from membrane disruption after incubation with chitosan-silver nanoparticles. Furthermore, the corresponding phase images (Figure 1-5 e and f) are unaffected by local topography and highlight variations in the tip-sample interaction which are consistent with

important modification in surface properties due to the damage of the bacterial cell integrity. Cross-sectional analysis in Figure 1-5 h and i demonstrates that the distinct holes formed in the bacteria biofilm originate from the discharge of bacterial content following the treatment with chitosan-silver nanocomposites.

### 5.3. SERS measurements

Figure 2-5 a and b shows the surface-enhanced Raman scattering (SERS) spectra collected from mixtures of 700  $\mu\text{l}$  silver colloid and 100  $\mu\text{l}$  *S. aureus* ( $10^5$  CFU/mL). For reference, the SERS spectrum of colloidal silver nanoparticles (without the addition of bacteria) is measured and no specific Raman signal is detected from it (Figure 2c-5). The subsequent analysis of the enhancement of the specific vibrational bands identifies the interaction between the bacterial cells and the silver surface and probes the biochemistry of the *S. aureus* cell surface [27]. The prominent band at  $741\text{ cm}^{-1}$  is characteristic for Gram-positive bacteria and originates from glycosidic ring vibration associated with the presence of polysaccharides on the cell surface. The bands at  $966$  and  $1035\text{ cm}^{-1}$  arise probably from the lipid layer components of the cell walls and membranes, and the  $1220$ - $1660\text{ cm}^{-1}$  region was previously assigned to amide I, II and III vibrations associated with protein backbone and carboxylic stretches. The bands at  $1090$  and  $1460\text{ cm}^{-1}$  can be attributed to the proteins' vibration modes.

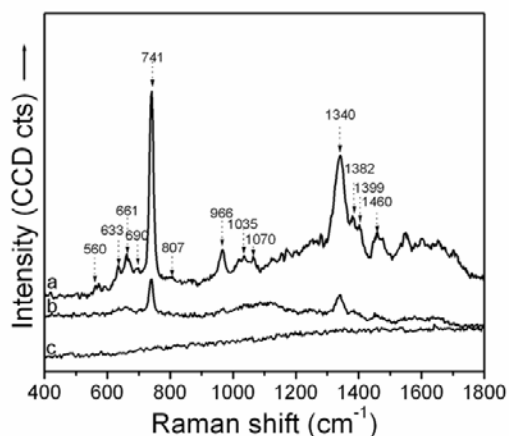


**Figure 2-5.** SERS spectra of *Staphylococcus aureus* obtained in solution with  $632.8$  excitation wavelengths. (a) with silver nanoparticles as SERS substrate, (b) with chitosan-silver nanocomposites as SERS substrate. The final concentration of bacterial sample was  $1.25 \times 10^4$  CFU/mL. (c) SERS spectrum of silver colloidal solution (without the addition of bacteria).

It is worth mentioning that a drastic decrease of the Raman signal is observed when the chitosan-silver nanocomposites are used as SERS substrate (Figure 2b-5). We can assume that the chitosan layer around the nanoparticle hinders the direct interaction between bacterial cells and metal core as well as the particles aggregation which results in a significant decrease of SERS signal.

## Conclusions

In this thesis I prepared, characterized and studied the optical properties and growth mechanisms of anisotropic chitosan noble-metal nanocomposites. Furthermore, I demonstrated the applicability of as synthesized nanoparticles in biomedical sensing, imaging and therapy.

- 1. We synthesized gold-chitosan nanocomposites of different sizes, shapes and spatial organization.**
- 2. We designed biocompatible plasmonic nanostructures based on chitosan and anisotropic silver nanoparticles with tunable plasmonic resonances.**
- 3. We developed a versatile plasmonic sensor in solution by merging two detection approaches: LSPR-SERS.**
- 4. We designed a novel, biocompatible SERS substrate based on small clusters of anisotropic silver nanoparticles embedded in a film of chitosan.**
- 5. We demonstrated that chitosan and silver nanoparticles act synergistically against two strains of Gram-positive methicillin resistant *Staphylococcus aureus*.**

## References

- [1] S. Link, M. A. El-Sayed. *Optical properties and ultrafast dynamics of metallic nanocrystals* Annu. Rev. Phys. Chem. **54** (2003) 331-366.
- [2] P. K. Jain, X. Huang, I. H. El-Sayed, M. A. P. El-Sayed. *Review of some interesting surface plasmon resonance-enhanced properties of noble metal nanoparticles and their applications to biosystems.* Plasmonics. **2** (2007) 107-118.
- [3] J. N. Anker, W. P. Hall, O. Lyandres, N. C. Shah, J. Zhao, R. P. Van Duyne. *Biosensing with plasmonic nanosensors.* Nat. Mater. **7** (2008) 442-453.
- [4] A. J. Haes, R. P. Van Duyne. *A nanoscale optical biosensor: sensitivity and selectivity of an approach based on the localized surface plasmon resonance of triangular silver nanoparticles.* J. Am. Chem. Soc. **124** (2002)10596–10604.
- [5] W. Xie, P. Qiu, C. Mao. *Bio-imaging, detection and analysis by using nanostructures as SERS substrates.* J. Mater. Chem. **21** (2011) 5190-5202.

- [6] M. Baia, S. Astilean, T. Iliescu. *Raman and SERS investigations of pharmaceuticals*. (2008) Berlin: Springer.
- [7] L.F.E. Cristobal, G.A.M. Castanon, R.E.M. Martinez, J.P.L. Rodriguez, N.P. Marin, J.F.R. Macias, F. Ruiz. Antibacterial effect of silver nanoparticles against *Streptococcus mutans*. *Mater. Lett.* **63** (2009)
- [8] J.S. Kim, E. Kuk, K. N. Yu, J. H. Kim, S. J. Park, H. J. Lee, S. H. Kim, Y.K. Park, Y. H. Park, C.Y. Hwang, Y. K. Kim, Y. S. Lee, D. H. Jeong, M. H. Cho. *Antimicrobial effects of silver nanoparticles*. *Nanomedicine: Nanotechnology, Biology, and Medicine* **3** (2007) 95–101.
- [9] J. R. Morones, J. L. Elechiguerra, A. Camacho, K. Holt, J.B. Kouri, J.T. Ramirez, M.J. Yacaman. *The bactericidal effect of silver nanoparticles*. *Nanotechnology* **16** (2005) 2346–2353.
- [10] M. Rinaudo. *Chitin and chitosan: Properties and applications*. *Prog. Polym. Sci.* **31** (2006) 603-632
- [11] M.N.V.Ravi Kumar, R.A.A.Muzzarelli, C.Muzzarelli, H.Sashiwa, A.J.Domb. *Chitosan Chemistry and Pharmaceutical Perspectives*. *Chem. Rev.* **104** (2004) 6017- 6084.
- [12] **M. Potara**, D. Maniu, S.Astilean. *The synthesis of biocompatible and SERS-active gold nanoparticles using chitosan*. *Nanotechnology*. **20** (2009) 315602 (7pp).
- [13] P. K. Jain, K. S. Lee, I. H. El-Sayed, M. A. El-Sayed. *Calculated absorption and scattering properties of gold nanoparticles of different size, shape, and composition: Applications in biological imaging and biomedicine*. *J. Phys. Chem. B* **110** (2006) 7238-7248
- [14] W. Xu, S. Xu, X. Ji, B. Song, H. Yuan, L. Mac, Y. Bai. *Preparation of gold colloid monolayer by immunological identification*. *Colloids Surf. B.* **40** (2005) 169-172.
- [15] **M. Potara**, A. Gabudean, S. Astilean. *Solution-phase, dual LSPR-SERS plasmonic sensors of high sensitivity and stability based on chitosan-coated anisotropic silver nanoparticles*. *J. Mater. Chem.* **21** (2011) 3625-3633.
- [16] I. Pastoriza-Santos, L. M. Liz-Marzan. *Colloidal silver nanoplates. State of the art and future challenges*. *J. Mater. Chem.* **18** (2008) 1724–1737.
- [17] M. C. Moulton, L. K. Braydich-Stolle, M. N. Nadagouda, S. Kunzelman, S. M. Hussain, R. S. Varma. *Synthesis, characterization and biocompatibility of “green” synthesized silver nanoparticles using tea polyphenols*. *Nanoscale*. **2** (2010) 763-770
- [18] G. Socrates. *Infrared and Raman Characteristic Group Frequencies* (2001) 3rd edn (Chichester: Wiley)
- [19] L. J. Sherry, R. Jin, C. A. Mirkin, G. C. Schatz, R. P. Van Duyne. *Localized surface plasmon resonance spectroscopy of single silver triangular nanoprisms*. *Nano Lett.* **6** (2006) 2060–2065.
- [20] X. Zou, S. Dong. *Surface-enhanced Raman scattering studies on aggregated silver nanoplates in aqueous solution*. *J. Phys. Chem. B.* **110** (2006) 21545–21550.
- [21] L. Rodriguez-Lorenzo, R. A. Alvarez-Puebla, F. J. Garcia de Abajo, L. M. Liz-Marzan. *Surface enhanced Raman scattering using star-shaped gold colloidal nanoparticles*. *J. Phys. Chem. C* **114** (2010) 7336–7340.
- [22] **M. Potara**, M. Baia, C. Farcau, S. Astilean, *Chitosan-coated anisotropic silver nanoparticles as a SERS substrate for single molecule detection*, *Nanotechnology* **23** (2012) Article number 055501(10pp).
- [23] B. Giese, D. McNaughton. *Surface-enhanced Raman spectroscopic and Density Functional Theory study of adenine adsorption to silver surfaces*. *J. Phys. Chem. B* **106** (2002) 101-112.
- [24] J. P. Camden, J. A. Dieringer, Y. Wang, D. J. Masiello, L. D. Marks, G. C. Schatz, R. P. Van Duyne. *Probing the structure of single-molecule surface-enhanced Raman scattering hot spots*. *J. Am. Chem. Soc.* **130** (2008) 12616-12617
- [25] L. Qi, Z. Xu, X. Jiang, C. Hu, X. Zou. *Preparation and antibacterial activity of chitosan nanoparticles*. *Carbohydr. Res.* **339** (2004) 2693–2700.
- [26] **M. Potara**, E. Jakab, A. Damert, O. Popescu, V. Canpean, S. Astilean, *Synergistic antibacterial activity of chitosan-silver nanocomposites on *Staphylococcus aureus**, *Nanotechnology* **22** (2011) Article number 135101 (9pp)
- [27] H. Chu, Y. Huang, Y. Zhao. *Silver nanorod arrays as a surface-enhanced Raman scattering substrate for foodborne pathogenic bacteria detection*. *Appl. Spectrosc.* **62** (2008) 922-931.